High-performance flexible all-solid-state asymmetric supercapacitors from nanostructured electrodes prepared by oxidation-assisted dealloying protocol

Ran Wang[a], Yanwei Sui[a, b*], Saifang Huang[b], Yuguang Pu[b], Peng Cao[b*]

[a] School of Materials Science and Engineering, China University of Mining and Technology, Xuzhou 221116, People's Republic of China

[b] Department of Chemical & Materials Engineering, University of Auckland, Private Bag 92019, Auckland 1142, New Zealand

* Correspondence authors. E-mail addresses: wyds123456@outlook.com (Y. Sui) or p.cao@auckland.ac.nz (P. Cao).

Abstract: Flexible all-solid-state energy storage devices that can function under considerably large mechanical deformation have shown great promise for portable electronics applications. However, conventional techniques are cumbersome in building cost-effective flexible all-solid-state energy storage devices, thus limiting their widespread applications. Here we report a flexible all-solid-state supercapacitor whose electrodes were prepared via a facile oxidation-assisted dealloying protocol for the first time. The electrodes demonstrate good flexibility and excellent performance. We assembled a prototype all-solid-state asymmetric supercapacitor (ASC) from the as-prepared Co_3O_4 flakes and γ-Fe_2O_3 nanoparticles as the positive and negative electrodes, respectively. The flexible ASC device possesses an extended operating voltage window of 1.7 V and a high energy density of 38.1 Wh/kg. We also demonstrated that four supercapacitor cells that were constructed in series illuminated 52 LEDs for at least 7 min. The ASC device has excellent power density and energy density that comparable to the art-of-the-state supercapacitors reported in the literature, and retains good charge and discharge performance under different bending conditions. The synthesis strategy reported here may be beneficial to the low-cost mass production of nanostructured electrode materials for energy storage applications.

Keywords: Electrodes; Asymmetric Supercapacitor; Dealloying Oxidation; Energy Storage Device; Flexibility

1. Introduction

Increasing demand for portable consumer and wearable electronics urges the development of novel energy storage devices that are lightweight, flexible, of high power and energy densities [1-3]. In the past decades, supercapacitors have been attracting significant interest attention due to their high power density, exceptionally long cycling lifetime, excellent stability during cycling, and excellent safety liability [4, 5]. Unfortunately, the energy density of commercially available supercapacitors is remarkably lower than those of batteries and fuel cells, which limits their application in next-generation portable devices [6]. Asymmetric supercapacitors (ASCs) are an effective approach for extending the operating voltage window of the powder sources [7-12]. The ASC generally consists of a battery-type Faradic electrode (cathode) as an energy source and a capacitor-type electrode (anode) as a power source. The ASC technology is expected to achieve an increased energy density and high cell voltage.

Despite great progress in improving the capacitance of cathode materials, the anode materials have been rarely investigated. Carbon-based nanomaterials are commonly used as anode in ASCs. However, the low specific capacitance of carbon materials severely limits the energy density for ASCs [13]. Metal oxide based anodes with nanostructures, such as MoO_3, Bi_2O_3 and Fe_2O_3, are promising electrode materials for ASCs because of their high specific capacitance, typically 2-3 times higher than that of carbon/graphite-based materials [14-16]. To prepare uniform metal oxide nanostructures, many strategies such as electrodeposition [17], hydrothermal

reduction [18], solvothermal synthesis [19], sol-gel method [20] have been developed. These methods include meticulous chemical steps, excessive use of organic chemicals and operation at high temperatures. Recently, dealloying – a selective dissolution of one or more elements in an alloy – is used to fabricate nanoporous metals for application in supercapacitors [21-23]. Lang *et al*. [24] have developed a nanoporous Au/MnO_2 electrode by the combination of chemical dealloying and electroless plating, where MnO_2 grows on the internal surface of nanoporous channels. The nanocomposite-based supercapacitor exhibits a specific capacitance of constituent MnO_2, which is close to the theoretical value. The metal/oxide hybrid material has very high specific capacitance and energy density. However, to the best of our knowledge, the fabrication of nanoporous metal oxide by oxidation-assisted dealloying method for supercapacitors is still in its infancy. Low-cost nanoporous metal oxides such as NiO, Cu_2O and Fe_2O_3 with tunable pore sizes are clearly in great demand for energy storage applications. In these metal oxides, the porous supports offer a three-dimensional conductive pathway, facilitating charge transport effectively, while nano-sized pore channels, serving as reservoirs of electrolytes, provide short ion diffusion distance and have low resistance. Additionally, nanoporous architectures offer large effective surface areas, improving its specific capacitance [25-27].

In this work we report a simple oxidation-assisted dealloying process to produce Co_3O_4 with a 3D interconnected porous framework for cathode material and γ-Fe_2O_3 nanoparticles for anode material. A flexible all-solid-state ASC was constructed based

on these low-cost Co_3O_4 and γ-Fe_2O_3 electrodes with KOH/poly vinyl alcohol (PVA) as electrolyte. The prototype device exhibited a high specific capacitance of 94.7 F/g at a current density of 0.7 A/g and an energy density of 38.1 Wh/kg.

2. Experimental section

2.1 Synthesis of the flexible Co_3O_4 positive electrode

The precursor ($Al_{65}Co_{35}$, at. %) was designed according to the nominal composition of a single-phase Al_5Co_2 intermetallic compound. Fig. S1 shows the Al–Co binary phase diagram. $Al_{65}Co_{35}$ ingots were prepared by arc-melting pure bulk metals (Al, 99.99 wt. %; Co, 99.99 wt. %) in an argon atmosphere. Then, the ingots (about 35 g) were melted by high-frequency induction heating in a quartz glass tube and melt-spun onto a copper roller at a circumferential speed of 1500 rpm in a controlled argon atmosphere (as shown in Fig. S3). The as-spun alloy ribbons obtained are about 20–40 μm thick, 3–5 mm wide, and several centimeters long. Subsequently, the alloy ribbons were ball-milled in an agate tank (150 mL) using a planetary ball mill (QM-3SP04, Nanjing, China) under ambient conditions at 300 rpm for 6h. The ball-to-ribbon weight ratio was maintained at 20:1.

The obtained $Al_{65}Co_{35}$ alloy powders were then dealloyed in a 0.2 wt. % NaOH aqueous solution at 20 °C for 48h. After dealloying, the powders were filtered with a filter paper and rinsed with distilled water for several times. The products were then dried in vacuum for 12h at 70 °C and nanostructured Co_3O_4 flakes resulted. The

flake-like Co_3O_4 powders (80 wt. %), carbon black (10 wt. %) and polyvinylidene-fluoride (PVDF, 10 wt. %) were weighed and mixed in a mortar. A small amount of N-methylpyrrolidone (NMP) was then added to form a homogeneous mixture. The resulting mixture was coated onto a 25mm × 15mm Ni-foam and was dried at 70 °C for 12h in vacuum. Finally, the positive electrode is pressed to 0.3 mm.

2.2 Fabrication of the flexible γ-Fe_2O_3 negative electrode

The precursor ($Al_{71}Fe_{29}$, at. %) was designed according to the nominal composition of a single-phase Al_5Fe_2 intermetallic compound. Fig. S2 shows the Al–Fe binary phase diagram. A similar procedure described in fabrication of Co_3O_4 was used to prepare $Al_{71}Fe_{29}$ powder. The obtained $Al_{71}Fe_{29}$ alloy powders were dealloyed in a 2 wt. % NaOH aqueous solution at 85 °C for 48h. An identical drying procedure as described previously was used to prepare γ-Fe_2O_3 powders. Using γ-Fe_2O_3 (80 wt. %), carbon black (10 wt. %) and PVDF (10 wt. %), the negative electrode 0.3 mm think was prepared, as per the procedures described in Section 2.1.

2.3 Assembly of the flexible all-solid-state supercapacitor

Polymeric PVA-KOH gel electrolyte was prepared by mixing 3 g KOH and 6 g PVA in 60 mL deionized water at 80 °C and stirring it using a magnetic stirrer until the solution became clear gel. Both positive and negative electrodes were dipped into the gel electrolyte solution for 3 min to absorb the gel electrolyte. After solidified at room temperature, two pieces of flexible electrodes were separated by the PVA-KOH gel

film were used to assemble a flexible all-solid-state Co_3O_4//γ-Fe_2O_3 supercapacitor. The schematic diagram of the fabrication process of the flexible ASC supercapacitor is shown in Fig. 1.

2.4 Materials characterization

The crystal structure of the as-synthesized products were characterized by a Bruker Advance Eco X-ray powder diffractometer (XRD) with Cu-Kα radiation (λ=1.5418 Å) in the 2θ range of 10° – 80°. The morphology and microstructure of the samples were studied by transmission electron microscopy (TEM, Tecnai G2 F20) and scanning electron microscopy (SEM, JEOL JSM-6700). X-ray photoelectron spectra (XPS) were recorded on a Thermo VG ESCALALAB 250 X-ray photoelectron spectrometer using Al Kα X-rays as the excitation source. The specific surface area was measured by the multipoint Brunauer-Emmett-Teller (BET) method at 77.3 K with a quanta-chrome NOVA4200e system. The pore size distributions (PSD) were obtained by means of the Barrett-Joyner-Halenda (BJH) equation using the adsorption isotherm branch.

2.5 Electrochemical performance measurements

Electrodes were tested on a CHI660E electrochemical workstation in a three-electrode electrochemical cell using a 1M KOH aqueous solution as electrolyte at room temperature. The Co_3O_4 electrode or γ-Fe_2O_3 electrode was used as the working electrode. A platinum plate and Ag/AgCl electrode were used as the counter and reference electrode, respectively. Cyclic voltammetry (CV) and galvanostatic

charge/discharge (GCD) tests were conducted at different scan rates and current densities. Electrochemical impedance spectra (EIS) were measured in the frequency range of 0.01 to 100000 Hz. The specific capacitance was derived from the discharge time as per the following equation [22]:

$$C=(I\cdot\Delta t)/(\Delta V\cdot m) \quad (1)$$

where I is the discharge current. Δt is the discharge time, ΔV represents the potential window and m is the mass of the electroactive materials.

The energy density (E) and power density (P) of the flexible all-solid-state ASC device were calculated using the following equations [22]:

$$E=C\Delta V^2/2 \quad (2)$$

$$P=E/\Delta t \quad (3)$$

3. Results and discussion

3.1 Characteristics of nanosized Co_3O_4 and γ-Fe_2O_3

The microstructure of the as-synthesized Co_3O_4 flakes is shown in Fig. 2a, where highly porous Co_3O_4 nanosheets are observed. The size of the pores in the Co_3O_4 nanosheets ranges from 100 to 500 nm (Fig. 2b). The highly porous channels and large specific areas are beneficial to energy storage devices. The hierarchical nature of the Co_3O_4 flakes is further presented in a typical TEM image (Fig. 2c). As shown in the HRTEM image, Fig. 2d, the interplanar spacing is 0.285 nm and 0.244 nm, corresponding to the (220) and (311) plane of Co_3O_4, respectively. This is well

consistent with its XRD pattern (Fig. 2e). All the noticeable diffraction peaks of XRD pattern can be well indexed to the cubic Co_3O_4 (JCPDS NO. 42-1467), whose space group is *Fd3m* (no. 227) with cell parameters *a*=*b*=*c*=8.084 Å [28]. XPS analysis in Fig. 2f reveals two peaks at 780.6 and 797.6 eV, which are characteristic spectral signals of $Co2p_{3/2}$ and $Co2p_{1/2}$ spin-orbit in Co_3O_4, respectively. The peaks at 787 and 803 eV in Fig. 2f are the two shake-up satellite peaks. The XPS spectra are in good agreement with the other reports [29, 30].

The morphology and microstructure of γ-Fe_2O_3 nanoparticles were analyzed by SEM and TEM. A large number of γ-Fe_2O_3 nanoparticles with various particle sizes are presented in Figs. 3a and 3b. The interplanar spacing measured from the HRTEM image is 0.252 nm, which matches closely to the (311) plane of the cubic γ-Fe_2O_3. The identification of γ-Fe_2O_3 is further confirmed by XRD and XPS. All the diffraction peaks in Fig. 3e can be well indexed to γ-Fe_2O_3 (JCPDS no. 39-1346). As shown in Fig. 3f, the two obvious peaks of XPS spectrum at 710.9 and 724.5 eV correspond to the $Fe2p_{3/2}$ and $Fe2p_{1/2}$ spin-orbit of γ-Fe_2O_3 [31, 32]. In addition to these two peaks, a satellite peak of weak intensity is visible at 718.9 eV.

The pore microstructure and specific surface area of both γ-Fe_2O_3 and Co_3O_4 are characterized with N_2 adsorption and desorption isotherms, as shown in Fig. S4. Two distinct regions are observed. At high relative pressures, a hysteresis loop associated with capillary condensation is observed. This corresponds to a Type IV isotherm,

indicating the existence of a typical mesoporous microstructure. As shown in Table S1, the BET surface area (S_{BET}) of γ-Fe_2O_3 and Co_3O_4 are 15.46 and 33.38 m^2 g^{-1}, respectively. Particle size distribution (PSD) analysis reveals that the BJH adsorption average pore diameters are 8.83 and 7.47 nm for γ-Fe_2O_3 and Co_3O_4, respectively.

Fig. 4a shows the CV curves of the Co_3O_4 electrode in the potential range of -0.2 to 0.5 V at different scan rates. The non-rectangular shape of these CV curves suggest that part of the capacitance originates from the pseudocapacitance of redox active Co_3O_4. An increased scan rate causes a positive shift of oxidation (anodic) peak and a negative shift of reduction (cathodic) peak. It is also noted that increasing scan rate leads to augmentation of the CV curve loop, suggesting excellent kinetics of interfacial Faradic redox reactions and fast transportation of ions and electrons. The previous reports proposed three reversible redox reactions Co(II) ↔ Co(III) ↔ Co(IV) in a basic electrolyte [33]. Fig. 4b shows the CV curves of γ-Fe_2O_3 at various scan rates in the potential range of -1.1 to -0.2 V. A pair of well-defined peaks at around -0.65 V for the anodic scan and -1.0 V for the cathodic scan can be clearly observed, which are ascribed to the reversible oxidation and reduction process between Fe^{3+} and Fe^{2+} as per $Fe_2O_3 + 3H_2O + 4e^- \leftrightarrow 2Fe(OH)_2 + 2OH^-$ [34]. It is noted that, nickel foam reacts with electrolyte in an alkaline environment may also contribute to the capacitance. In our case, such contribution is negligible (see the CV curves of a bare foam nickel electrode in Fig. S9).

Fig. 4c presents the galvanostatic charging/discharging (GCD) curves of Co_3O_4 at various current densities in the potential range of -0.2 to 0.5 V. It is known that a Faradic redox reaction is commonly associated with a double-layer charge/discharge process [33, 35]. The GCD curves of γ-Fe_2O_3 at various current densities (Fig. 4d) exhibit obvious plateaus at about -0.65 V and -1.0 V respectively, at a low current density (0.7 or 1 A/g). These plateaus occur at the redox potentials of γ-Fe_2O_3. As expected, the plateaus are unnoticeable at higher current densities (Fig. 4d). Besides, from the CV and GCD curves, no obvious hydrogen evolution is observed, due to the high hydrogen evolution overpotential of the γ-Fe_2O_3. Thus, it can be concluded that the potential of -0.2 to -1.0 V is a safe potential window for the as-synthetic γ-Fe_2O_3. Such a broad potential window is beneficial for enhancing the energy density of the as-fabricated two-electrode ASC.

The variations of the specific capacitance of these two electrode materials against current density are plotted together in Fig. 5a for easy comparisons. The specific (gravimetric) capacitance of the Co_3O_4 is 410 F/g at a current density of 0.7 A/g, which doubles that of γ-Fe_2O_3 (187 F/g). These measured specific capacitances are much lower than the theoretical specific capacitances. The galvanostatic charging/discharging behaviors were further evaluated after 5000 cycles. Fig. 5b shows the specific capacitance retention of Co_3O_4 at a current density of 5 A/g in the potential rage of -0.2 to 0.5 V and γ-Fe_2O_3 at a current of 1 A/g in the potential rage of -1.1 to -0.2 V. It is demonstrated that Co_3O_4 and γ-Fe_2O_3 maintain 80.5% and 93.2%

of their initial capacitance after 5000 cycles, respectively.

The Nyquist plots of the Co_3O_4 and γ-Fe_2O_3 electrodes are presented in Fig. 5c and 5d, where the insets show the semicircle at the high frequency end. The high-frequency arc indicates the charge transfer limiting process, which results from the double-layer capacitance and the charge-transfer resistance at the interface between electrode and electrolyte solution. The straight line with a slope close to 45° at low-frequency is caused by the adsorption of ions onto the electrode surface [36]. The equivalent series resistance (ESR) of both Co_3O_4 and γ-Fe_2O_3 electrodes shows a very small resistance, indicating a good ionic response, and is consistent with the small IR drop of the discharge curves. The major difference after 5000 cycles is the semicircle in the high frequency region, suggesting that cycling has caused an increased charge-transfer resistance and pseudocapacitance deterioration. Nevertheless, the synthesized Co_3O_4 and γ-Fe_2O_3 have demonstrated high capacitance, excellent rate capability and good cycling stability, and therefore being promising electrodes for flexible all-solid-state ASC device applications.

3.2 Assessment of all-solid-state ASC device

To further demonstrate the feasibility of the Co_3O_4 and γ-Fe_2O_3 electrodes for real applications, all-solid-state ASC devices were assembled and tested, with Co_3O_4 and γ-Fe_2O_3 being the positive electrode and negative electrode, respectively (Fig. 6b). Fig. 6a shows the CV curves of the Co_3O_4 and γ-Fe_2O_3 electrodes at 100 mV/s. It is obvious that the Co_3O_4 electrode has a stable operating voltage window between -0.2

to 0.5 V, while the negative γ-Fe_2O_3 electrode has a stable voltage window between -1.1 and -0.2 V.

The assembled Co_3O_4//γ-Fe_2O_3 ASC device was subjected to CV assessment (Fig. 6c). A sharp peak appears at approximately 1.35 V during the forward scan, while at 0.7 V during backward scan. The energy storage mechanism based on Faradic reaction is explained as follows. During charging of the as-assembled all-solid-state ASC device, the anode γ-Fe_2O_3 undergoes the reduction process as $2Fe_2O_3 + 6H_2O + 4e^- \leftrightarrow 4Fe(OH)_2 + 4OH^-$ at the potential of -1.0 V, and the cathode Co_3O_4 is oxidized following the process of $Co_3O_4 + 4OH^- \leftrightarrow 3CoO_2 + 2H_2O + 4e^-$ at 0.2 to 0.4 V. Fig. 6c also shows the CV cures at various scan rates from 10 mV/s to 150 mV/s. Furthermore, the CV and GCD curves of the ASC device collected at different voltage windows are shown in Fig. S5a and S5b. It is observed that the Faradic reactions occur more efficiently with the increase of operating potential to 1.7 V. Fig. 6d presents the GCD curves of the flexible all-solid-state ASC at various current densities. These curves are nonlinearly correlated with the potential, indicating pseudocapacitive behaviors.

As shown in Fig. 6e, the specific capacitance values of the all-solid-state ASC device are 94.7, 87.1, 78.5, 74.1, 67.1, 55.9, 49.4 and 41.2 F/g at current densities of 0.7, 1, 1.5, 2, 3, 5, 7 and 10 A/g, respectively. The cycling durability of the all-solid-state ASC device was further evaluated at a current density of 4 A/g for 5000 cycles. It

illustrates that the device retains 80.1% of the initial capacitance, revealing its excellent long-term cyclic stability (Fig. S6). Typical Nyquist plots of the all-solid-state device after the 1st and 5000th cycles are presented in Fig. 6f. The semi-circle size increment from the 1st to the 5000th cycles is very small, indicating that the nanostructures were well maintained and preserved overall with little structural change after 5000 cycles. The positive and negative electrodes were subjected to SEM observations, which confirm that the structure of the active materials has good stability after 5000 cycles (Fig. S7). In addition, the increase of the Warburg resistance after 5000 cycles can be attributed to the loss of adhesion of some active materials, blocking the diffusion pathways of ions during the charge-discharge process.

A single cell of the ASC device has successfully achieved an operating voltage of up to 1.7 V, higher than that of the commercial alkaline batteries (1.5 V). Nevertheless, the voltage provided by a single cell is still unable to meet the power and energy requirements for practical microelectronics applications. In order to test its practical applicability, two ASC devices were assembled in series (Fig. 7a) and in parallel (Fig. 7d). The tandem device and multiple device were evaluated by CV and GCD measurements. As shown in Figs. 7b and 7c the potential window is extended from 1.7 V for a single device to 3.4 V for two ASC devices connected in series. Meanwhile, the product current (represented by the area under the CV curves) and the charge/discharge time at the same current density are essentially the same for the

tandem device as individual cells. Figs. 7e and 7f show the CV and GCD curves of the two ASC devices connected in parallel, respectively. As compared with a single ASC device, the output current of the assembled parallel ASC devices is increased by a factor of two under the same voltage window of 0 to 1.7 V. The discharge time is approximately two times longer than that of a single device. These results demonstrate that the electrochemical performance of the Co_3O_4//γ-Fe_2O_3-ASC devices is stable and reproducible for integral assembly. This provides opportunities for larger power density storage by connecting multiple device units on demand.

To further evaluate the flexibility of this design, an all-solid-state ASC was assembled using the Co_3O_4 nanosheets as positive electrode and the γ-Fe_2O_3 as negative electrode with PVA/KOH as the gel electrolyte. As for the fabricated ASC, the charge balance between the two electrodes follows the relationship of $q_+=q_-$. According to the equation of $q=I\times t=C\times V\times m$, the charge stored by each electrode (q) depends on the specific capacitance (C), operating voltage window during the charge/discharge cycles excluding IR drop (V), and the mass of active materials (m). The mass ratio between the positive and negative electrodes is expressed as follows: $m_+/m_-=C_-\times V_-/C_+\times V_+$ [37, 38].

A schematic diagram of the flexible ASC is shown in Fig. 8a. Electrochemical tests were conducted at a scan rate of 100 mV/s on the assembled flexible device that was bent up to 180°. As shown in Fig. 8b, the CV curves with different bending angles

only differed slightly. It is worth noting that the specific capacitance of the device was maintained throughout the entire bending process. This is evidenced in the inset of Fig. 8b, where a red LED was powered by a flexible device under normal and bent states. The gravimetric Ragone plots of the Co_3O_4//γ-Fe_2O_3 ASC is presented in Fig. 8c, where the performance of the devices are compared with those of the recently reported ASCs and commercially available energy-storage devices [39-44]. Our device demonstrates a maximum gravimetric energy density of 38.1 Wh/kg at an operating potential of 1.7 V. Its maximum power density was 8.5 kW/kg at 10 A/g. These values are comparable to those of the recent state-of-the-art devices (Fig. 8c). The maximum energy density reported here is greater than that of NiO//α-Fe_2O_3 ASC [42] and Co_3O_4//Co_3O_4 symmetric supercapacitor (SSC) [44], but smaller than that of α-Fe_2O_3/PEDOT//α-Fe_2O_3/PEDOT SSC [40]. Additionally, our flexible all-solid-state ASC device has exhibited much higher maximum power density than the recently reported devices MnO_2// Fe_2O_3 [41].

The good performance of the flexible all-solid-state Co_3O_4//γ-Fe_2O_3 ASC can be attributed to the following reasons: (1) the asymmetric device has a high operation voltage and specific capacitance; (2) the unique nanosheets and highly porous structure of Co_3O_4 facilitate a large interfacial contact region between the electrolytes. The excellent electrochemical performance of the flexible all-solid-state Co_3O_4//γ-Fe_2O_3 ASC makes it promising for the next generation energy storage. The optimization of the dealloying method herein reported and the exploration of the size

effect of the active materials fall beyond the scope of this research, but they are worth future investigations. Fig. 8d demonstrates that the devices worn on the wrist were able to illuminate 52 red LEDs. When four single units were connected in series, they illuminated 52 red LEDs for over 7 min (Fig. 8e1 to 8e5), demonstrating its suitability as a flexible energy storage device for practical applications.

4. Conclusions

In summary, the Co_3O_4 nanosheets and γ-Fe_2O_3 nanoparticles were synthesized through a facile oxidation-assisted dealloying method. An all-solid-state flexible ASC was assembled from Co_3O_4 positive electrode and γ-Fe_2O_3 negative electrode on a flexible polymeric substrate. Except for PVA/KOH as the gel electrolyte, no other materials including binder, separator or any packaging material were used. The assembled ASC exhibited a long cycle life (80.1% device capacitance retention over 5000 cycles) and ultrahigh gravimetric energy density of 38.1 Wh/kg, about tenfold higher than those of the state-of-the-art commercial supercapacitors. The Co_3O_4//γ-Fe_2O_3 flexible all-solid-state ASCs device delivers a maximum power density of up to 8.5 kW/kg, a value comparable to that of typical commercially available supercapacitors and more than one order of magnitude higher than the power density of lithium batteries. The flexible all-solid-state ASC can be integrated either in series or in parallel to meet the energy and power needs in various potential applications, including portable flexible optoelectronics, sensors and energy devices. Our device could bridge the energy density gap between micro-batteries and

micro-supercapacitors for miniaturized portable electronics. This facile electrode design may open up new opportunities for development of other metal oxide electrodes for high-performance electrochemical storage device applications.

Acknowledgements

This research was supported by National Natural Science Foundation of China (Contract Nos. 51671214 and 51601220), Science and Technology Project of Jiangsu Province, China (BY.2016026-05).

References

[1] X.H. Lu, G.M. Wang, T. Zhai, M.H. Yu, S.L. Xie, Y.C. Ling, C.L. Liang, Y.X. Tong, Y. Li, Stabilized TiN Nanowire Arrays for High-Performance and Flexible Supercapacitors, Nano Lett. , 12 (2012) 5376-5381.

[2] X. Pu, L.X. Li, M.M. Liu, C.Y. Jiang, C.H. Du, Z.F. Zhao, W.G. Hu, Z.L. Wang, Wearable Self-Charging Power Textile Based on Flexible Yarn Supercapacitors and Fabric Nanogenerators, Adv. Mater. , 28 (2016) 98-105.

[3] H. Pang, Y.Z. Zhang, Z. Run, W.Y. Lai, W. Huang, Amorphous nickel pyrophosphate microstructures for high-performance flexible solid-state electrochemical energy storage devices, Nano Energy, 17 (2015) 339-347.

[4] Y. Li, X.Q. Yan, X. Zheng, H.N. Si, M.H. Li, Y.C. Liu, Y.H. Sun, Y.R. Jiang, Y. Zhang, Fiber-shaped asymmetric supercapacitors with ultrahigh energy density for flexible/wearable energy storage, J Mater Chem A, 4 (2016) 17704-17710.

[5] X. Zheng, X.Q. Yan, Y.H. Sun, Y. Li, M.H. Li, G.J. Zhang, Y. Zhang, Band alignment engineering for high-energy-density solid-state asymmetric supercapacitors with TiO_2 insertion at the ZnO/$Ni(OH)_2$ interface, J Mater Chem A, 4 (2016) 17981-17987.

[6] Q. Wang, J. Yan, Z.J. Fan, Carbon materials for high volumetric performance supercapacitors: design, progress, challenges and opportunities, Energy Environ. Sci. , 9 (2016) 729-762.

[7] X. Zhou, Q. Chen, A.Q. Wang, J. Xu, S.S. Wu, J. Shen, Bamboo-like Composites of V_2O_5/Polyindole and Activated Carbon Cloth as Electrodes for All-Solid-State Flexible Asymmetric Supercapacitors, ACS Appl. Mat. Interfaces 8(2016) 3776-3783.

[8] H. Pang, Y.Z. Zhang, W.Y. Lai, Z. Hu, W. Huang, Lamellar $K_2Co_3(P_2O_7)_2{\cdot}2H_2O$ nanocrystal whiskers: High-performance flexible all-solid-state asymmetric micro-supercapacitors via inkjet printing, Nano Energy, 15 (2015) 303-312.

[9] C. Zhou, Y.W. Zhang, Y.Y. Li, J.P. Liu, Construction of High-Capacitance 3D CoO@Polypyrrole Nanowire Array Electrode for Aqueous Asymmetric

Supercapacitor, Nano Lett. , 13 (2013) 2078-2085.

[10] Y.R. Jiang, X. Zheng, X.Q. Yan, Y. Li, X. Zhao, Y. Zhang, 3D architecture of a graphene/$CoMoO_4$ composite for asymmetric supercapacitors usable at various temperatures, J. Colloid Interface Sci. , 493 (2017) 42-50.

[11] Y.Z. Zhang, J.H. Zhao, J. Xia, L.L. Wang, W.Y. Lai, H. Pang, W. Huang, Room temperature synthesis of cobalt-manganese-nickel oxalates micropolyhedrons for high-performance flexible electrochemical energy storage device, Sci Rep-Uk, 5 (2015).

[12] Y.Z. Zhang, T. Cheng, Y. Wang, W.Y. Lai, H. Pang, W. Huang, A Simple Approach to Boost Capacitance: Flexible Supercapacitors Based on Manganese Oxides@MOFs via Chemically Induced In Situ Self-Transformation, Adv. Mater. , 28 (2016) 5242-5248.

[13] Q.T. Qu, P. Zhang, B. Wang, Y.H. Chen, S. Tian, Y.P. Wu, R. Holze, Electrochemical Performance of MnO_2 Nanorods in Neutral Aqueous Electrolytes as a Cathode for Asymmetric Supercapacitors, J. Phys. Chem. C 113 (2009) 14020-14027.

[14] J. Chang, M. Jin, F. Yao, T.H. Kim, V.T. Le, H. Yue, F. Gunes, B. Li, A. Ghosh, S. Xie, Y.H. Lee, Asymmetric Supercapacitors Based on Graphene/MnO_2 Nanospheres and Graphene/MoO_3 Nanosheets with High Energy Density, Adv. Funct. Mater. , 23 (2013) 5074-5083.

[15] H.W. Wang, Z.J. Xu, H. Yi, H.G. Wei, Z.H. Guo, X.F. Wang, One-step preparation of single-crystalline Fe_2O_3 particles/graphene composite hydrogels as high performance anode materials for supercapacitors, Nano Energy, 7 (2014) 86-96.

[16] T.P. Gujar, V.R. Shinde, C.D. Lokhande, S.H. Han, Electrosynthesis of Bi_2O_3 thin films and their use in electrochemical supercapacitors, J. Power Sources 161 (2006) 1479-1485.

[17] H. Lee, J. Kang, M.S. Cho, J.B. Choi, Y. Lee, MnO_2/graphene composite electrodes for supercapacitors: the effect of graphene intercalation on capacitance, J. Mater. Chem. , 21 (2011) 18215-18219.

[18] P.H. Yang, Y. Ding, Z.Y. Lin, Z.W. Chen, Y.Z. Li, P.F. Qiang, M. Ebrahimi, W.J. Mai, C.P. Wong, Z.L. Wang, Low-Cost High-Performance Solid-State Asymmetric Supercapacitors Based on MnO_2 Nanowires and Fe_2O_3 Nanotubes, Nano Lett. , 14 (2014) 731-736.

[19] Y.Y. Yang, Y.R. Liang, Z.Y. Zhang, Y.D. Zhang, H.Y. Wu, Z.A. Hu, Morphology well-controlled synthesis of NiO by solvothermal reaction time and their morphology-dependent pseudocapacitive performances, J. Alloys Compd. , 658 (2016) 621-628.

[20] X.Y. Wang, X.Y. Wang, W.G. Huang, P.J. Sebastian, S. Gamboa, Sol-gel template synthesis of highly ordered MnO_2 nanowire arrays, J. Power Sources 140 (2005) 211-215.

[21] L. Zhang, Y.W. Zhan, H.D. Bian, Z. Li, C.K. Tsang, C. Lee, H. Cheng, S.W. Shu, Y.Y. Li, J. Lu, Electrochemical dealloying using pulsed voltage waveforms and its application for supercapacitor electrodes, J. Power Sources 257 (2014) 374-379.

[22] H.J. Qiu, Y. Ito, M.W. Chen, Hierarchical nanoporous nickel alloy as three-dimensional electrodes for high-efficiency energy storage, Scr. Mater. , 89 (2014) 69-72.

[23] P.C. Chen, S.J. Hsieh, J. Zou, C.C. Chen, Selectively dealloyed Ti/TiO_2 network nanostructures for supercapacitor application, Mater. Lett. , 133 (2014) 175-178.

[24] X.Y. Lang, A. Hirata, T. Fujita, M.W. Chen, Nanoporous metal/oxide hybrid electrodes for electrochemical supercapacitors, Nat. Nanotechnol. , 6 (2011) 232-236.

[25] S. Liu, J.K. Feng, X.F. Bian, J. Liu, H. Xu, The morphology-controlled synthesis of a nanoporous-antimony anode for high-performance sodium-ion batteries, Energy Environ. Sci. , 9 (2016) 1229-1236.

[26] P. Simon, Y. Gogotsi, Materials for electrochemical capacitors, Nat. Mater. , 7 (2008) 845-854.

[27] P.H. Yang, W.J. Mai, Flexible solid-state electrochemical supercapacitors, Nano

Energy, 8 (2014) 274-290.

[28] T. Sen, N.G. Shimpi, S. Mishra, R. Sharma, Polyaniline/γ-Fe_2O_3 nanocomposite for room temperature LPG sensing, Sensor Actuat B-Chem, 190 (2014) 120-126.

[29] F.H. Su, X.M. Lv, M.H. Miao, High-Performance Two-Ply Yarn Supercapacitors Based on Carbon Nanotube Yarns Dotted with Co_3O_4 and NiO Nanoparticles, Small, 11 (2015) 854-861.

[30] J. Xu, Q.F. Wang, X.W. Wang, Q.Y. Xiang, B. Hang, D. Chen, G.Z. Shen, Flexible Asymmetric Supercapacitors Based upon Co_9S_8 Nanorod//Co_3O_4@RuO_2 Nanosheet Arrays on Carbon Cloth, ACS Nano, 7 (2013) 5453-5462.

[31] L.S. Xiao, M. Schroeder, S. Kluge, A. Balducci, U. Hagemann, C. Schulzad, H. Wiggers, Direct self-assembly of Fe_2O_3/reduced graphene oxide nanocomposite for high-performance lithium-ion batteries, J Mater Chem A, 3 (2015) 11566-11574.

[32] N.S. Arul, D. Mangalaraj, R. Ramachandran, A.N. Grace, J.I. Han, Fabrication of CeO_2/Fe_2O_3 composite nanospindles for enhanced visible light driven photocatalysts and supercapacitor electrodes, J Mater Chem A, 3 (2015) 15248-15258.

[33] J. Yan, T. Wei, W.M. Qiao, B. Shao, Q.K. Zhao, L.J. Zhang, Z.J. Fan, Rapid microwave-assisted synthesis of graphene nanosheet/Co_3O_4 composite for supercapacitors, Electrochim. Acta 55 (2010) 6973-6978.

[34] Q.Q. Tang, W.Q. Wang, G.C. Wang, The perfect matching between the low-cost Fe_2O_3 nanowire anode and the NiO nanoflake cathode significantly enhances the energy density of asymmetric supercapacitors, J Mater Chem A, 3 (2015) 6662-6670.

[35] S.K. Meher, G.R. Rao, Ultralayered Co_3O_4 for High-Performance Supercapacitor Applications, J. Phys. Chem. C 115 (2011) 15646-15654.

[36] X.M. Liu, Q. Long, C.H. Jiang, B.B. Zhan, C. Li, S.J. Liu, Q. Zhao, W. Huang, X.C. Dong, Facile and green synthesis of mesoporous Co_3O_4 nanocubes and

their applications for supercapacitors, Nanoscale, 5 (2013) 6525-6529.

[37] Z. Gao, W.L. Yang, J. Wang, N.N. Song, X.D. Li, Flexible all-solid-state hierarchical $NiCo_2O_4$/porous graphene paper asymmetric supercapacitors with an exceptional combination of electrochemical properties, Nano Energy, 13 (2015) 306-317.

[38] D.Z. Kong, C.W. Cheng, Y. Wang, J.I. Wong, Y.P. Yang, H.Y. Yang, Three-dimensional Co_3O_4@C@Ni_3S_2 sandwich-tructured nanoneedle arrays: towards high-performance flexible all-solid-state asymmetric supercapacitors, J Mater Chem A, 3 (2015) 16150-16161.

[39] A.V. Shinde, N.R. Chodankar, V.C. Lokhande, A.C. Lokhande, T. Ji, J.H. Kim, C.D. Lokhande, Highly energetic flexible all-solid-state asymmetric supercapacitor with Fe_2O_3 and CuO thin films, Rsc Adv, 6 (2016) 58839-58843.

[40] J.W. Park, W. Na, J. Jang, Hierarchical core/shell Janus-type α-Fe_2O_3/PEDOT nanoparticles for high performance flexible energy storage devices, J Mater Chem A, 4 (2016) 8263-8271.

[41] G.S. Gund, D.P. Dubal, N.R. Chodankar, J.Y. Cho, P. Gomez-Romero, C. Park, C.D. Lokhande, Low-cost flexible supercapacitors with high-energy density based on nanostructured MnO_2 and Fe_2O_3 thin films directly fabricated onto stainless steel, Sci Rep-Uk, 5 (2015) ARTN 12454.

[42] S.W. Zhang, B.S. Yin, Z.B. Wang, F. Peter, Super long-life all solid-state asymmetric supercapacitor based on NiO nanosheets and α-Fe_2O_3 nanorods, Chem. Eng. J. , 306 (2016) 193-203.

[43] Q.Y. Liao, N. Li, S.X. Jin, G.W. Yang, C.X. Wang, All-Solid-State Symmetric Supercapacitor Based on Co_3O_4 Nanoparticles on Vertically Aligned Graphene, ACS Nano, 9 (2015) 5310-5317.

[44] X.Y. Liu, Y.Q. Gao, G.W. Yang, A flexible, transparent and super-long-life supercapacitor based on ultrafine Co_3O_4 nanocrystal electrodes, Nanoscale, 8 (2016) 4227-4235.

Figures

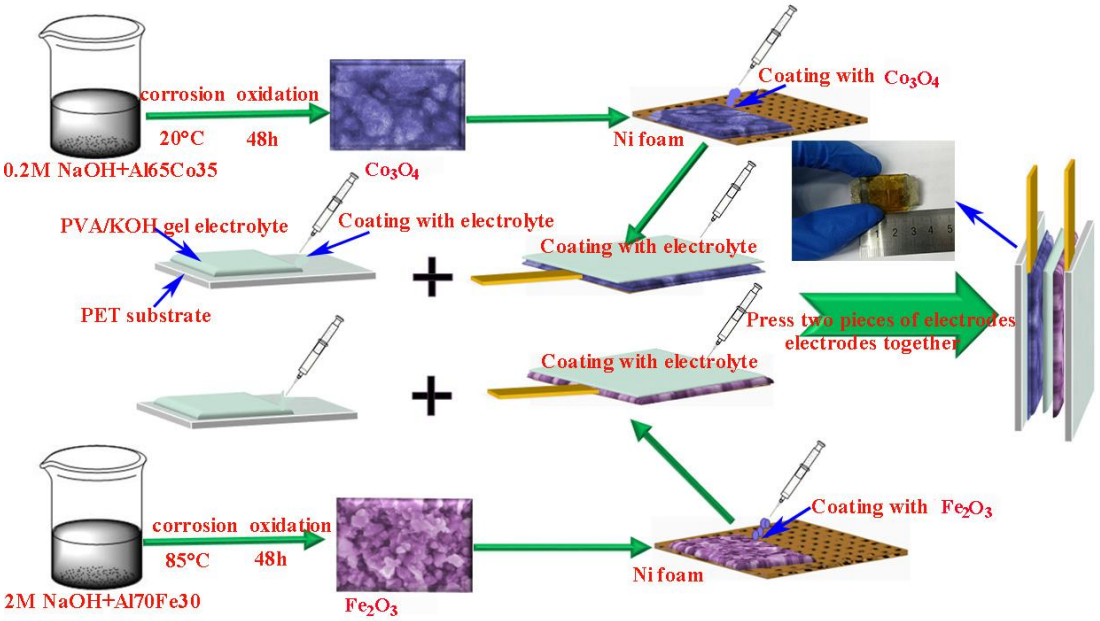

Fig. 1 Schematic diagram of the fabrication of Co_3O_4//γ-Fe_2O_3 flexible solid-state supercapacitor.

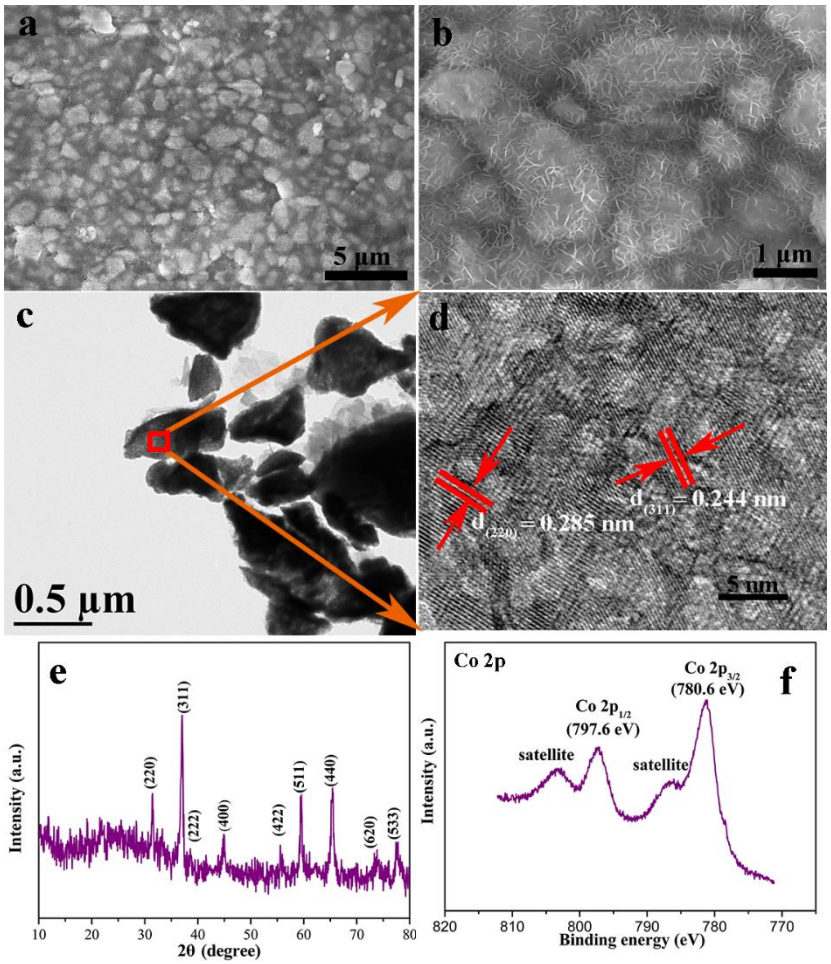

Fig. 2 (a) and (b) SEM images with different magnifications of Co_3O_4 nanosheets. (c) TEM bright field image, and (d) HRTEM images (e) XRD pattern and (f) Co 2p XPS spectrum.

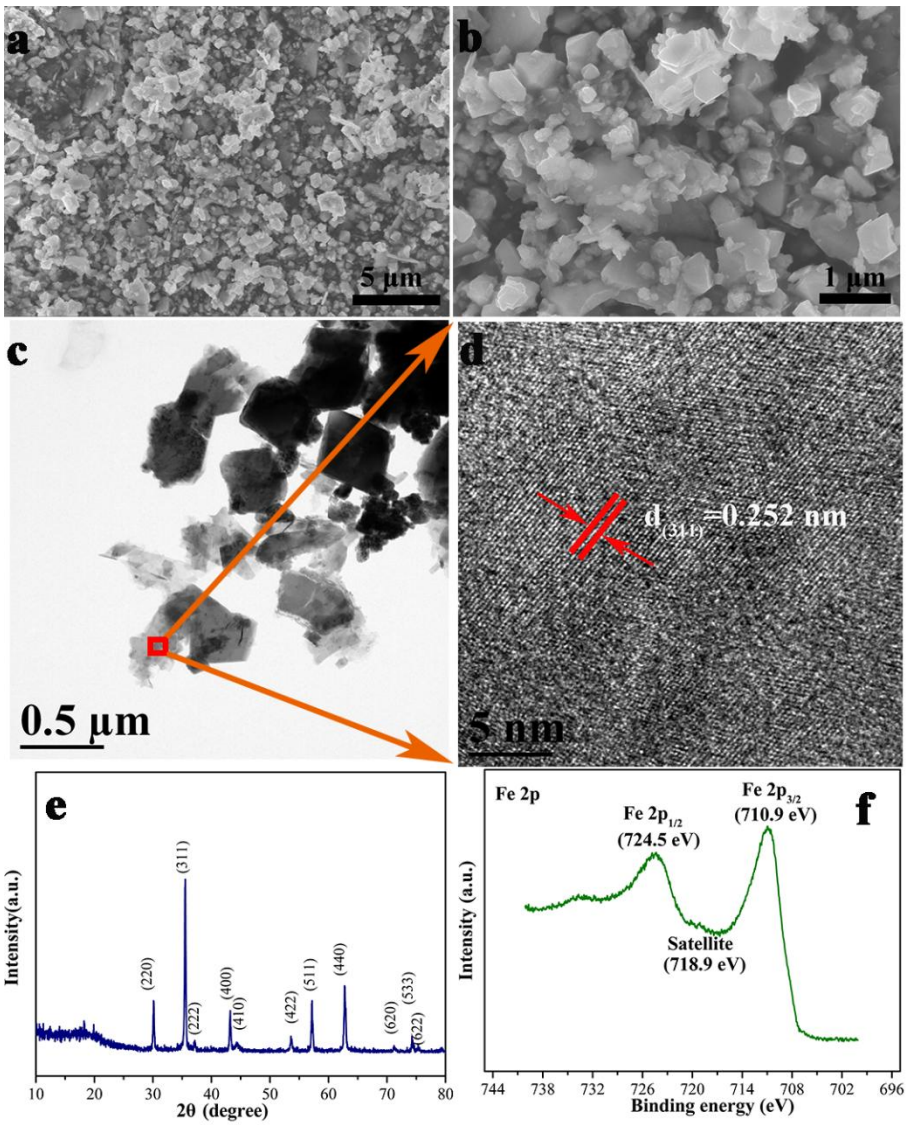

Fig. 3 (a) and (b) SEM images with different magnifications of γ-Fe_2O_3 nanoparticles. (c) TEM bright field image. (d) HRTEM image. (e) XRD pattern and (f) Fe 2p XPS spectrum.

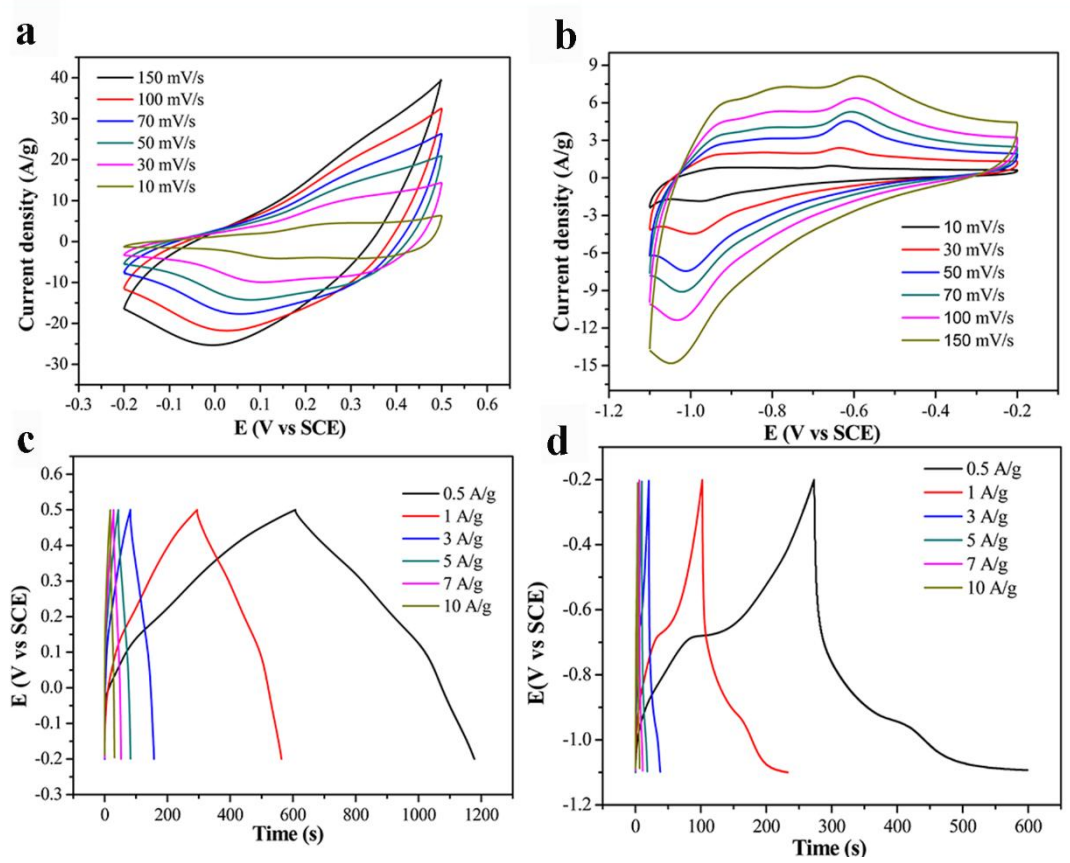

Fig. 4 Electrochemical performance of the Co_3O_4 and γ-Fe_2O_3 electrodes in a three-electrode setup in a 1 M KOH solution. CV curves of (a) Co_3O_4 and (b) γ-Fe_2O_3 electrodes at various scan rates between 10 to 150 mV/s. (c) and (d) Galvanostatic charging/discharging curves of Co_3O_4 and γ-Fe_2O_3 electrodes at different current densities ranging from 0.5 to 10A/g.

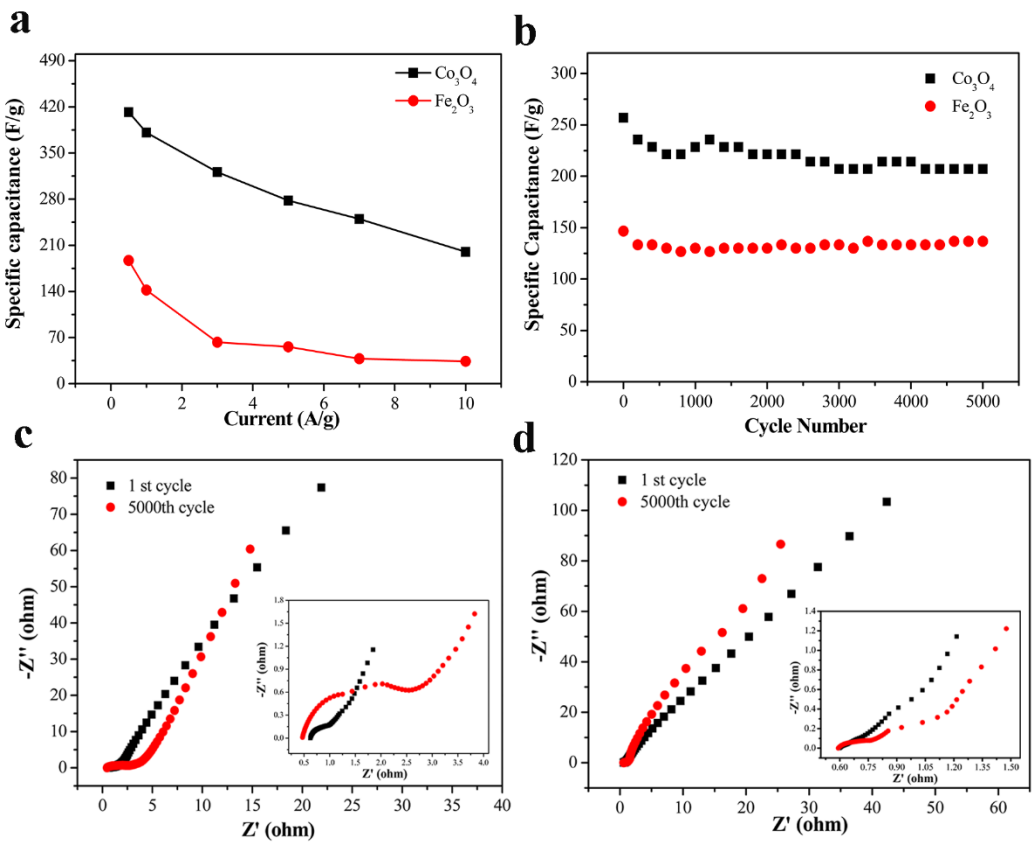

Fig. 5 Electrochemical performance of the Co_3O_4 and γ-Fe_2O_3 electrodes, evaluated by the three-electrode measurement in 1 M KOH. (a) Specific capacitance of Co_3O_4 and γ-Fe_2O_3 electrodes at different current densities. (b) Cycling performance of Co_3O_4 electrode at a current density of 5 A/g and γ-Fe_2O_3 electrode at a current density of 1 A/g. (c) and (d) Nyquist plots of the Co_3O_4 and γ-Fe_2O_3 electrodes before and after 5000 cycles, the inset is an enlarged section of the Nyquist plots in the very high frequency region.

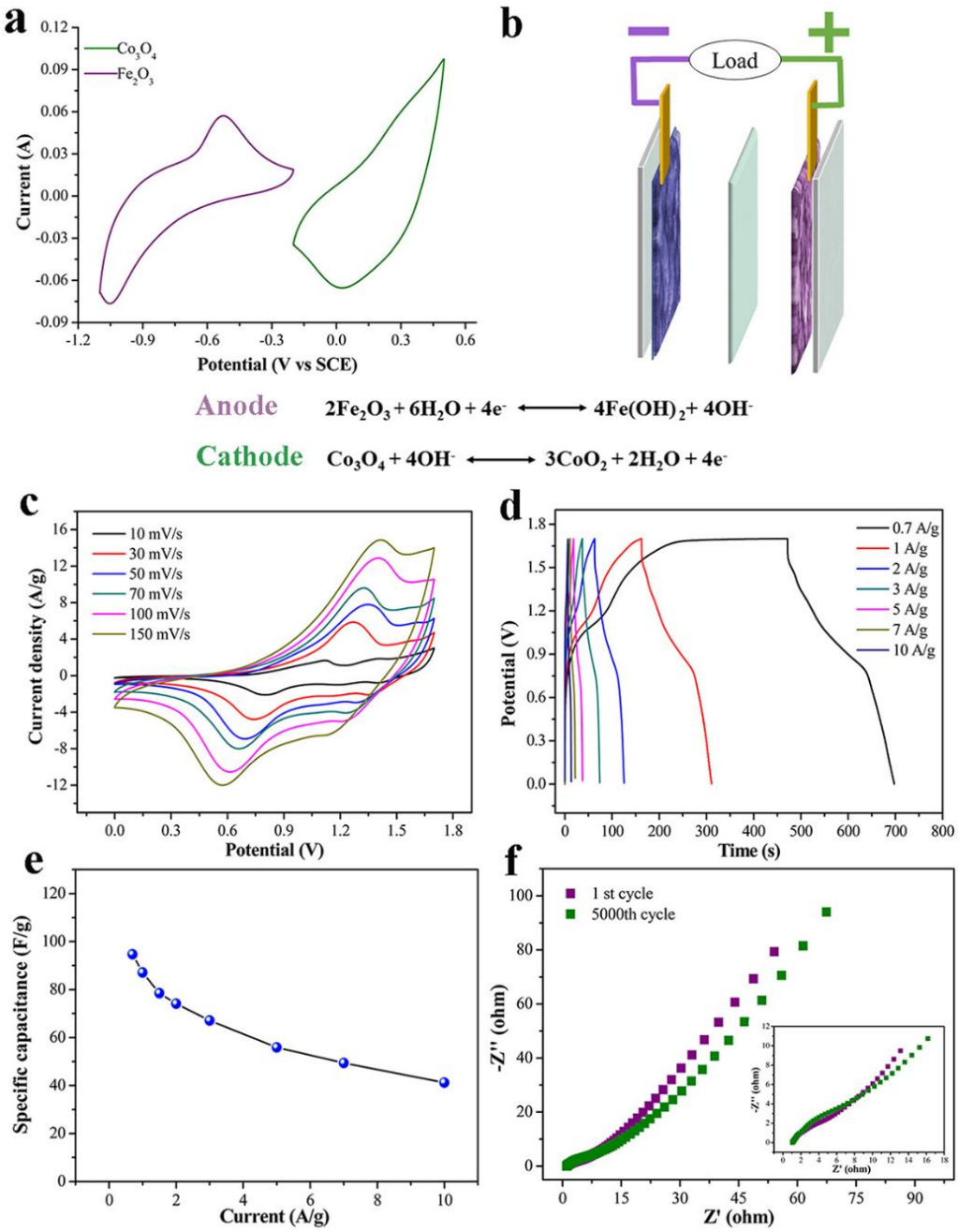

Fig. 6 (a) CV cures of γ-Fe_2O_3 and Co_3O_4 electrodes at a scan rate of 100 mV/s. (b) Schematic diagram of the as-assembled flexible all-solid-state ASC. Electrochemical performance assessment of the flexible all-solid-state ASC in terms of: (c) CV curves at different scan rates between 0 and 1.7 V. (d) GCD curves at current densities from 0.7 A/g to 10 A/g. (e) specific capacitance at different current densities. (f) Nyquist plots before and after 5000 cycles, the inset is the enlarged section in the high frequency region.

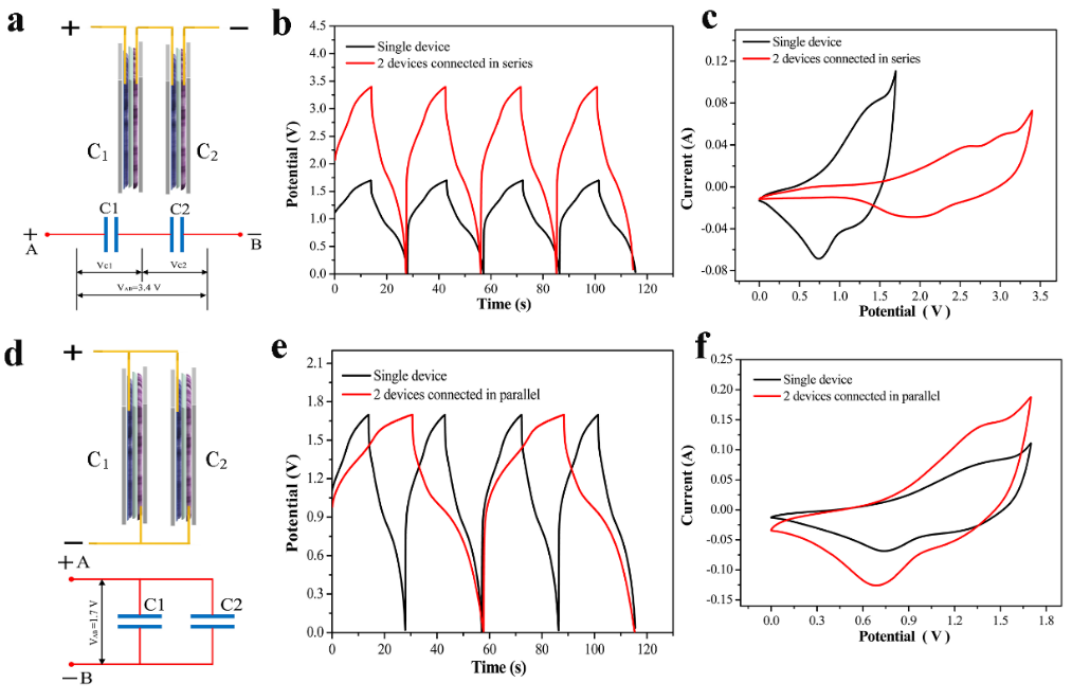

Fig. 7 Electrochemical performances of ASC devices in series and parallel circuits. (a) Illustration of two ASC devices connected in series and its corresponding circuit diagram. (b) GCD curves of two ASC devices connected in series. A single device is shown for comparison. (c) CV curves of a single ASC device and two ASC devices connected in series. (d) Illustration of two ASC devices connected in parallel and its corresponding circuit diagram. (e) GCD curves of two ASC devices connected in parallel. A single device is shown for comparison. (f) CV curves of a single ASC device and two ASC devices connected in parallel.

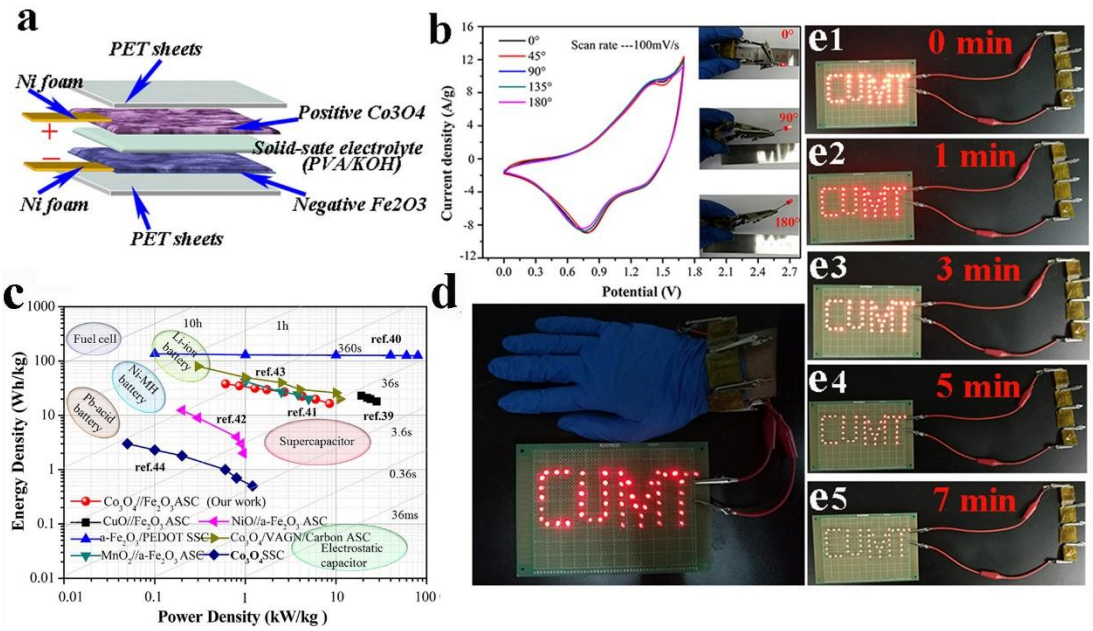

Fig. 8 (a) Schematic illustration of Co_3O_4//γ-Fe_2O_3 flexible solid-state ASCs device. (b) CV curves collected for the Co_3O_4//γ-Fe_2O_3-ASC under different bending conditions. The inset is the digital photograph of a red LED (LED, the lowest working potential is about 1.8 V) powered by a flexible ASCs device under normal and bent states. (c) Gravimetric Ragone plots of energy density *vs* average power density for our devices in comparison with other state-of-art ASCs. (d) and (e) Photographs showing that four supercapacitors in series can light up a 52-LEDs displayer for more than 7 minutes.